An Improved Modulation Strategy Without Current Zero-Crossing Distortion and Control Method for Vienna Rectifier

Wenjie Zhu, *Member, IEEE*, Xuewu Li, Xiaoya Cao, Yunfei Li, and Keliang Zhou, *Senior Member, IEEE*

***Abstract*—Vienna rectifier with simple structure, which has gained popularity in recent years for ac to dc power conversion for many industrial applications such as electric vehicle charging systems and uninterrupted power system (UPS) systems, accomplishes the operation of unit power factor. However, the distortion of the input current near the zero-crossing point is a puzzle that will increase the current harmonic content. In this article, the cause of the zero-crossing distortion is analyzed, and an improved space vector pulsewidth modulation modulation strategy is proposed. Moreover, the sliding mode control for the outer voltage loop and the phase compensation multiresonance control for the inner current loop is proposed to improve the dynamic response performance of the dc side and achieve zero-error control of the ac side. Simulation and experimental results verify the effectiveness of the proposed modulation scheme and control strategy.**

***Index Terms*—Harmonic suppression, phase compensated multiresonance (PCMPR) controller, Vienna rectifier, zero crossing distortion.**

I. Introduction

THE Vienna rectifier has become a hot research topic owing to its low voltage stress, few switching devices, and high power density. It is widely used in new energy development and applications, high-power charging systems, and UPS systems [1], [2], [3], [4], [5].

It is a very important requirement for VIENNA rectifier that the frequency and phase of the input current should be the same as the voltage. Thus, the modulation strategy is one of the key technologies, which is directly related to the quality of waveforms and the stability of the whole control system. The carrier-based pulse width modulation (CBPWM) [6] is widely used in three-level topologies, which is easy to implement, but there are large ripples and low dc voltage utilization rates. The discontinuous pulsewidth modulation (DPWM) [7], [8], [9] is a common modulation strategy for the Vienna rectifier, however, the neutral current appears large fluctuations under DPWM. Compare with these modulation strategies, the space vector pulse width modulation (SVPWM) [10], [11] not only improves the voltage utilization rate but also is easier to realize digitally and adjust easily.

However, the Vienna rectifier has the inherent current zero-crossing distortion problem, which will increase the total harmonic distortion (THD) of the grid-side current. In order to solve this problem, Yao et al. [12] proposed a method of changing the combination of vector states, but it adds extra computation and the suppression effect on current zero-crossing distortion is limited when the modulation index exceeds a certain value. Miao et al. [13] presented a controller-based compensation method based on the model for traditional SVPWM and CBPWM to suppress current zero-crossing distortion. However, the current zero-crossing distortion caused by modulation should be considered in the design of the controller and the effect of controller delay should also be calculated. Wang et al. [14] proposed a hybrid SVM modulation for a two-channel parallel Vienna rectifier, but its specific control methods are not described in detail.

As the core of power electronics systems, the control strategy is increasingly prominent in research. Several control schemes have been presented for the Vienna rectifier with a unity power factor. PI control [15] is a common control strategy for power electronic switching circuits, but it is difficult to track the zero-error of the ac side and it is slow to track the dynamic response of the dc side. Hysteresis control [16] is easy to implement, nevertheless, its switching frequency instability will affect the stability of the system. Model predictive control [17], [18], [19], [20] can combine modulation with control, but it has the problem of control delay. Sliding mode control [21] has a fast dynamic response and is common in solving nonlinear problems. Rajendran et al. [2] proposed a voltage-oriented controller, the reactive and unstable active currents are counteracted. Thus, many control

Manuscript received 20 January 2023; revised 27 April 2023 and 25 June 2023; accepted 22 July 2023. Date of publication 4 August 2023; date of current version 23 October 2023. This work was supported in part by the National Natural Science Foundation of China under Grant 61673305, in part by Shandong Provincial Natural Science Foundation under Grants ZR2023ME138 and ZR2022ZD38, in part by Shandong Province Higher Educational Science and Technology Program under Grant J15LN37, and in part by the Key Research and Development of Qingdao science and Technology Plan under Grant 22-3-3-hygg-30-hy. Recommended for publication by Associate Editor B. McGrath. *(Corresponding author: Wenjie Zhu.)*

Wenjie Zhu, Xuewu Li, and Yunfei Li are with the Qing Dao University of Technology, Qingdao 266000, China (e-mail: zhuwenjie@qut.edu.cn; lixuewu202112@163.com; 1286696583@qq.com).

Xiaoya Cao is with the School of Information and Control Engineering, Qing Dao University of Technology, Qingdao 266000, China (e-mail: cxy1712013234@163.com).

Keliang Zhou is with the School of Automation, Wuhan University of Technology, Wuhan 430070, China (e-mail: keliang.zhou@whut.edu.cn).

Color versions of one or more figures in this article are available at https://doi.org/10.1109/TPEL.2023.3302130.

Digital Object Identifier 10.1109/TPEL.2023.3302130

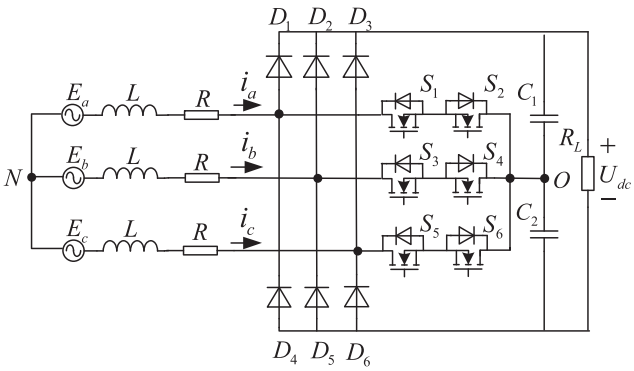

Fig. 1. Topology of the Vienna rectifier.

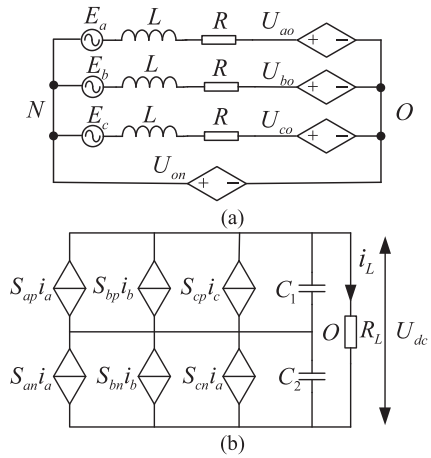

Fig. 2. Equivalent circuit of the Vienna rectifier.

strategies have been successfully applied in the control of voltage outer loop in rectifiers. In recent years, proportional resonance (PR) control [19], [22], [23] becomes a popular control strategy, which can have infinite gain at the resonant frequency and realize zero error tracking of the ac side. However, a single PR control cannot suppress all harmonics appearing in the current, so multiple PR controllers are connected in parallel to suppress harmonics at specific frequencies, but the phase lag increases as the number of PR controller increases.

In this article, an improved SVPWM was proposed to eliminate the grid-side current zero-crossing distortion. In order to suppress the current harmonic distortion effectively and improve the dynamic response speed of the system, a control strategy combining phase compensated multiresonance (PCMPR) control and a variable index approach law sliding mode control is developed for Vienna rectifier. In the current inner loop, compared with the common phase compensation methods, the PCMPR controller can compensate for the lag phase angle at specific frequencies to better maintain the stability of the system. And the compensation angle is derived by analyzing the mathematical model of Vienna rectifier. In the voltage outer loop, a variable index approaching law sliding mode control is proposed to improve the dynamic response speed of the system, and it eliminates the chatter of the system near the sliding surface. The effectiveness of the modulation and control strategies was verified under both ideal and weak grids.

The rest of this article is organized as follows. The mathematical model of the Vienna rectifier is established in Section II. Section III introduces the principle of zero-crossing distortion in detail and proposes an improved SVPWM modulation strategy to suppress current zero-crossing distortion. In Section IV, the proposed control method with suppressing current harmonics and improving dynamic response speed is proposed. Section V gives the simulation and experimental verifications of the proposed modulation strategy and control method. Finally, Section VI concludes this article.

II. Mathematic Model of the Vienna Rectifier

The schematic of the Vienna rectifier is shown in Fig. 1. $E_{\rm a}$, $E_{\rm b}$, $E_{\rm c}$ is the three-phase input voltage, L is the inductor on the ac side, R is the equivalent internal resistance, $i_{\rm a}$, $i_{\rm b}$, $i_{\rm c}$ are the input currents, C_1 and C_2 are the dc capacitances, and S_1–S_6 are the six power switch tubes.

During the whole operating state of the three-phase Vienna rectifier, the dc voltage has three values of $-U_{\rm dc}/2$, 0 and $+U_{\rm dc}/2$. Therefore, the switching function $S_{\rm ij}$ is supposed as

$$S_{\rm ij}=\begin{cases}0 & i=a,b,c\\ 1 & {\rm j=p,o,n}\end{cases}. \tag{1}$$

According to (1), the three-phase voltage loop equation can be obtained by Kirchhoff's Voltage Law (KVL), $U_{\rm ao}$, $U_{\rm bo}$, $U_{\rm co}$ are the voltage across the switch tube, $U_{\rm on}$ is the voltage between the midpoint of the capacitor and the grid neutral point

$$\begin{cases}E_a=L\frac{di_a}{dt}+Ri_a+U_{ao}+U_{\rm on}\\ E_b=L\frac{di_b}{dt}+Ri_b+U_{bo}+U_{\rm on}\\ E_c=L\frac{di_c}{dt}+Ri_c+U_{co}+U_{\rm on}.\end{cases} \tag{2}$$

Due to three-phase voltage symmetry, $E_a+E_b+E_c=0$, $i_a+i_b+i_c=0$, the common-mode voltage can be obtained

$$U_{\rm on}=-\frac{1}{3}\left(U_{ao}+U_{bo}+U_{co}\right). \tag{3}$$

According to the circuit relation, (4) can be obtained, where $S_{\rm ap}$, $S_{\rm bp}$, $S_{\rm cp}$, $S_{\rm an}$, $S_{\rm bn}$, $S_{\rm cn}$ are the switching functions, $U_{\rm C1}$, $U_{\rm C2}$ are the voltage of capacitances

$$\begin{cases}U_{ao}=S_{ap}U_{c1}-S_{an}U_{c2}\\ U_{bo}=S_{bp}U_{c1}-S_{bn}U_{c2}\\ U_{co}=S_{cp}U_{c1}-S_{cn}U_{c2}.\end{cases} \tag{4}$$

As shown in Fig. 2, the equivalent circuit in the *abc* coordinate system can be drawn.

The mathematical model of the VIENNA rectifier in the *abc* coordinate system is very complex and the parameters interact with each other, which makes the controller design difficult. Therefore, the mathematical model in the *abc* coordinate system can be converted to the $\alpha\beta$ coordinate system by the clark matrix.

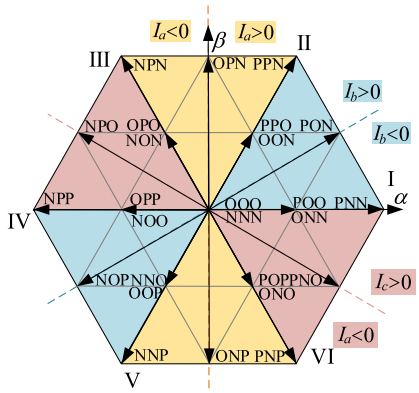

Fig. 3. Space voltage vector distribution of Vienna rectifier.

The mathematical model in the $\alpha\beta$ coordinate is

$$\begin{bmatrix} L\frac{di_\alpha}{dt} \\ L\frac{di_\beta}{dt} \\ C_1\frac{dU_{\mathrm{dc1}}}{dt} \\ C_2\frac{dU_{\mathrm{dc2}}}{dt} \end{bmatrix} = \begin{bmatrix} -R & 0 & -S_{\alpha p} & S_{\alpha n} \\ 0 & -R & -S_{\beta p} & S_{\beta n} \\ S_{\alpha p} & S_{\beta p} & -\frac{1}{R_L} & -\frac{1}{R_L} \\ -S_{\alpha n} & -S_{\beta n} & -\frac{1}{R_L} & -\frac{1}{R_L} \end{bmatrix} \begin{bmatrix} i_\alpha \\ i_\beta \\ U_{\mathrm{dc1}} \\ U_{\mathrm{dc2}} \end{bmatrix} + \begin{bmatrix} E_\alpha \\ E_\beta \\ 0 \\ 0 \end{bmatrix}. \tag{5}$$

Similarly, the mathematical model in the dq coordinate system is

$$\begin{bmatrix} L\frac{di_d}{dt} \\ L\frac{di_q}{dt} \\ C_1\frac{dU_{\mathrm{dc1}}}{dt} \\ C_2\frac{dU_{\mathrm{dc2}}}{dt} \end{bmatrix} = \begin{bmatrix} -R & \omega L & -S_{dp} & S_{dn} \\ -\omega L & -R & -S_{qp} & S_{qn} \\ S_{dp} & S_{qp} & -\frac{1}{R_L} & -\frac{1}{R_L} \\ -S_{dn} & -S_{qn} & -\frac{1}{R_L} & -\frac{1}{R_L} \end{bmatrix} \begin{bmatrix} i_d \\ i_q \\ U_{\mathrm{dc1}} \\ U_{\mathrm{dc2}} \end{bmatrix} + \begin{bmatrix} E_d \\ E_q \\ 0 \\ 0 \end{bmatrix}. \tag{6}$$

III. Improved SVPWM Modulation Strategy Without Zero Crossing Distortion

The Vienna rectifier space vector distribution is composed of 27 switching states with different sizes and directions. Its spatial voltage vector distribution is shown in Fig. 3. The whole voltage vector distribution space is divided into a large sector every 60°, and each large sector is divided into six small sectors, where the dotted line represents the three-phase current crossing zero.

The single-phase equivalent circuit for the Vienna rectifier in the ac side is illustrated in Fig. 4. Due to the small inductance R, the E_{k} can be obtained

$$E_k = L\frac{di_k}{dt} + U_{ko} + U_{\mathrm{on}}, \quad k = a, b, c. \tag{7}$$

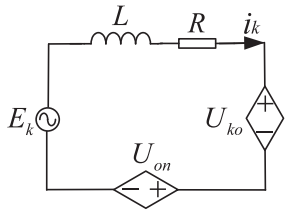

Fig. 4. Single-phase equivalent circuit for the Vienna rectifier.

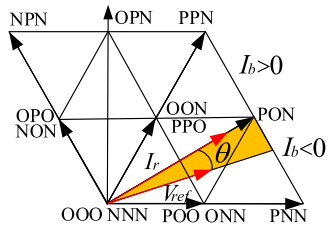

Fig. 5. Relative position of the reference voltage and the input current vector.

The three-phase modulated wave can be equivalent to the sum of common-mode component and sine wave, which can be expressed in [24]

$$V_{rk} = V_k + [-rV_a + (r-1)V_c + 2r - 1], \quad \mathrm{k} = \mathrm{a}, \mathrm{b}, \mathrm{c} \tag{8}$$

where V_{rk} is the equivalent three-phase modulated wave, V_{k} is the sinusoidal component, which amplitude is the modulation ratio m, r is the allocation coefficient of the redundancy vector, and the other terms are the injected common mode components.

According the mean equivalent model of state space, U_{ko} can be expressed as

$$U_{ko} = \frac{U_{\mathrm{dc}}}{2}V_{rk}, \quad k = a, b, c. \tag{9}$$

By substituting (3), (8), and (9) into (7), the inductor voltage can be written.

When the current is in the same sign as the modulated waveform

$$L\frac{di_k}{dt} = E_k - \frac{U_{\mathrm{dc}}}{2}V_k, \quad k = a, b, c. \tag{10}$$

When the current is in different sign as the modulated waveform

$$L\frac{di_k}{dt} = E_k + \frac{U_{\mathrm{dc}}}{2}\left(\frac{V_k}{3} + \frac{4}{3}V_{com}\right), k = a, b, c. \tag{11}$$

Since E_{k} and V_{k} are small when the current crosses near zero, the (11) can be simplified as

$$L\frac{di_k}{dt} \approx \frac{U_{\mathrm{dc}}}{2}\frac{4}{3}V_{com}. \tag{12}$$

According to (10)–(12), the common mode component will not affect the inductor voltage when the input current is in the same sign as the modulated waveform, and the inductor voltage will be influenced by the common-mode component when the current is in the different sign as the modulated waveform.

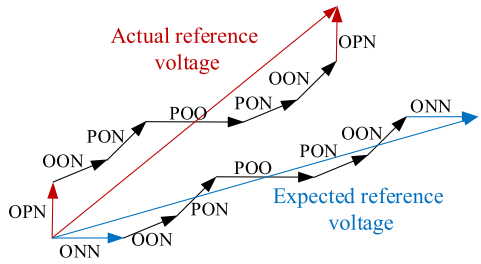

Fig. 6. Synthesis of reference voltage vectors.

The reference voltage vector V_{ref} and the input current vector I_{r} near the zero crossing of phase B with their relative position are shown in Fig. 5.

Due to the inductor voltage vector, the Vienna rectifier reference voltage vector will lag behind the input current vector

$$\frac{e_k\angle 0^\circ - v_k\angle\theta}{Z} = i_k\angle 0^\circ, \quad k=a,b,c. \tag{13}$$

The deviation angle θ can be calculated as

$$\theta = \tan^{-1}\left(\frac{-\omega L \times i_K}{e_K - R\times i_K}\right), \quad k=a,b,c. \tag{14}$$

When the modulation wave and the input current have opposite signs, the inductor voltage is far less than 0 due to the existence of common mode component, which will cause the synthesis errors of reference voltage vector and hinder the input current from negative to positive crossing. The synthesis of reference voltage vectors is shown in Fig. 6. The sign of the modulation wave is the same as that of the input current after crossing the zero line, and the inductor voltage is not related to the common mode component, the input current will quickly cross the zero line.

The common-mode component will hinder the current from crossing zero for conventional SVPWM due to the modulated wave sign cannot be guaranteed to be the same as the input current sign near the zero-crossing line, so the zero-crossing distortion will occur. The current tracking error and the rectifier system stability will be affected as the cumulative error increases. To eliminate the zero-crossing distortion of the Vienna rectifier, the period of the zero-switching state is increased near the zero-crossing point of current to keep the switches ON, so as to eliminate the reverse voltage drop on the inductor. In order to prevent the duty cycle from mutating, each switching cycle can be gradually reduced or increased and the zero-switching period should keep for enough time. Since the rotation angle of the composite vector within a period is 2π, the angle θ_0 occupied by each switching period can be expressed as

$$\theta_0 = \frac{2\pi T_s}{T_b} \tag{15}$$

where T_{S} is one switching cycle and T_{b} is a line-frequency cycle.

TABLE I
COMPENSATION VOLTAGE IN HALF POWER FREQUENCY

Range	Specific θ	compensation voltage
$\frac{\pi}{6}+\theta\sim\frac{\pi}{6}$	$\frac{\pi}{6}+\theta+(n-1)\theta_0 \sim\frac{\pi}{6}+\theta+n\theta_0$	$-\frac{n}{K}\mathrm{V}_{bref}$
	$\frac{\pi}{6}+\theta+K\theta_0\sim\frac{\pi}{6}$	$-\mathrm{V}_{bref}$
$\frac{\pi}{2}+\theta\sim\frac{\pi}{2}$	$\frac{\pi}{2}+\theta+(n-1)\theta_0 \sim\frac{\pi}{2}+\theta+n\theta_0$	$-\frac{n}{K}\mathrm{V}_{aref}$
	$\frac{\pi}{2}+\theta+K\theta_0\sim\frac{\pi}{2}$	$-\mathrm{V}_{aref}$
$\frac{5\pi}{6}+\theta\sim\frac{5\pi}{6}$	$\frac{5\pi}{6}+\theta+(n-1)\theta_0 \sim\frac{5\pi}{6}+\theta+n$	$-\frac{n}{K}\mathrm{V}_{cref}$
	$\frac{5\pi}{6}+\theta+K\theta_0\sim\frac{5\pi}{6}$	$-\mathrm{V}_{cref}$

According to (15), it can be concluded that the number of switching cycles N to be adjusted can be expressed as

$$N = \frac{\theta}{2\pi}\frac{T_b}{T_s} = \frac{\arctan\left(\frac{-\omega L * i_K}{e_K - r * i_K}\right)}{2\pi}\frac{T_b}{T_s}. \tag{16}$$

It can be seen from (16) that the number of switching cycles is related to T_{s} and the line-frequency. The higher the switching frequency is, the more switching cycles will be adjusted. Table I shows the size of the compensation component within half a power frequency cycle, where K is adjusted appropriately by the change of N to ensure the continuous change of the duty cycle. n is a natural number in the range of [1, K].

The conventional SVPWM and improved SVPWM are shown in Fig. 7. It can be seen that the zero-switching period is increased and the duty cycle changes gradually near the zero crossing of the modulated wave.

IV. CONTROL STRATEGY FOR VIENNA RECTIFIER

A. Design of Current Controller

It is well known that the PI controller can track the dc signals without static error in the dq coordinate system, and the PR controller can track the ac signals without static error in the $\alpha\beta$ coordinate system. Based on the mathematical model in dq and $\alpha\beta$ frame, the control parameters of axis α and axis β are independent, and the control strategies in $\alpha\beta$ frame remove complex decoupling operations.

The transfer function of PR controller can be expressed as

$$G(s) = K_p + \frac{2K_r\omega_c s}{s^2 + 2\omega_c s + \omega_0^2} \tag{17}$$

where ω_0 is the resonant frequency, ω_{c} is the bandwidth, and K_{r} denotes the gain of resonant controller.

In practical applications, the grid is usually not ideal, especially in weak grid conditions, the harmonics in the grid cannot be ignored. Compared with the ideal grid, the weak grid has two main characteristics: 1) the weak grid impedance is not ignorable

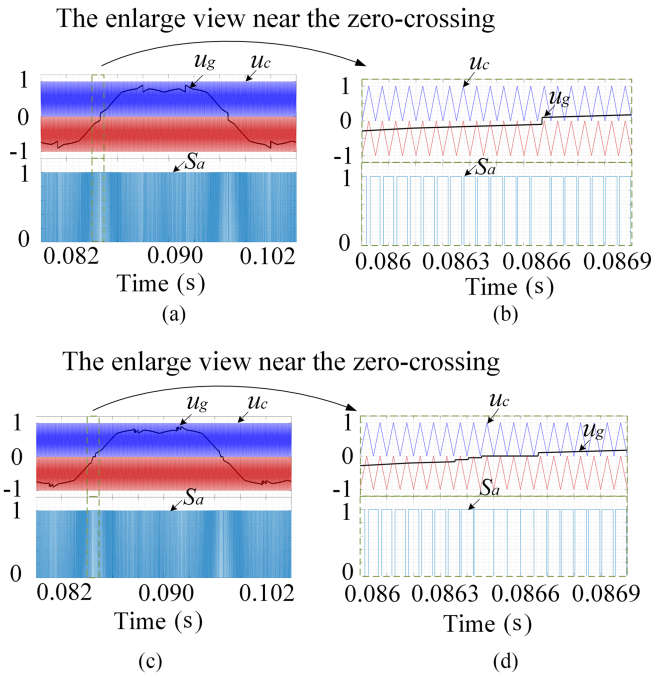

Fig. 7. Modulated wave under conventional SVPWM and improved SVPWM. (a) Modulated wave in a line-frequency cycle under conventional SVPWM. (b) Enlarged view of modulated wave near zero crossing under conventional SVPWM. (c) Modulated wave in a line-frequency cycle under improved SVPWM. (d) Enlarged view of modulated wave near zero crossing under improved SVPWM.

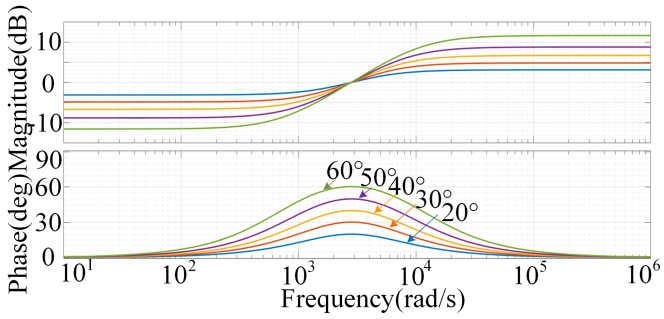

Fig. 8. Bode diagram of the lead compensator with different compensate angles θ.

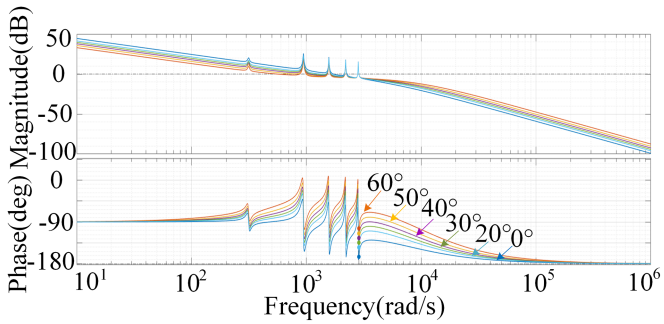

Fig. 9. Bode diagram of the current inner loop with lead compensator.

and 2) the weak grid contains a large number of background harmonics. High-order harmonics (third, fifth, seventh) are injected in the input current of the Vienna rectifier due to the distortion of the grid voltage [25], [26], which will damage the input current quality. Thus, the resonance controller can be connected in parallel to suppress the corresponding harmonics. The transfer function of multiresonance controller can be expressed as

$$R(s) = \sum \frac{2K_n\omega_c s}{s^2 + 2\omega_c s + \omega_n^2}, n = 1, 3, 5 \ldots \tag{18}$$

where K_{n} denotes the gain of multiresonance controller and the resonant frequency $\omega_{\mathrm{n}} = n\omega_0$.

However, due to the phase lag of the digital control delay and the controlled object, as the increase of number of PR controllers connected in parallel, the phase lag of closed-loop system becomes more and more obvious and the system becomes more and more unstable. Therefore, it is necessary to compensate the phase of the multiresonance controller. The phase compensator can be divided into three types: 1) lead-lag compensator, 2) proportional differential compensator, and 3) direct angle compensator.

The lead compensator can be expressed as

$$G_n(s) = K_n \frac{s + a\omega_1}{s + \omega_1} \tag{19}$$

where K_{n} denotes the gain of lead compensator.

The maximum lead angle φ_{n} and the maximum lead angle frequency ω_{n} are, respectively, as shown in

$$\varphi_n = \arcsin \frac{1-a}{1+a} \tag{20}$$

$$\omega_n = \omega_1 \sqrt{a}. \tag{21}$$

Fig. 8 shows the bode diagram of the lead compensator with different compensation angles. It can be seen that the lead compensator can correct the phase characteristics of the target band without affecting the phase characteristics of the other bands. In a system where multiple resonance controllers are connected in parallel, it is necessary to add a lead compensator at each resonant frequency, which makes the design of the system parameters more complicated. As the frequency of the system increases, the phase lag of the closed-loop system becomes more and more obvious. Therefore, the complexity of parameter design can be reduced by adding a lead compensator to the highest resonant controller. However, as shown in Fig. 9, with the increase of compensation angle, the influence of the phase lead compensator on the amplitude of other resonant frequencies is increasing. Moreover, the phase lead compensator needs to be redesigned when a new resonant controller is added to the system.

In addition to the phase lead compensator, the phase of the system can also be compensated by adding a proportional differentiation compensator. The resonant controller with the addition

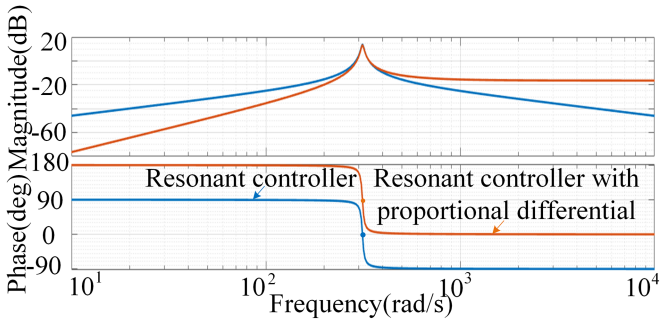

Fig. 10. Bode diagram of resonant controller with proportional differentiation compensator.

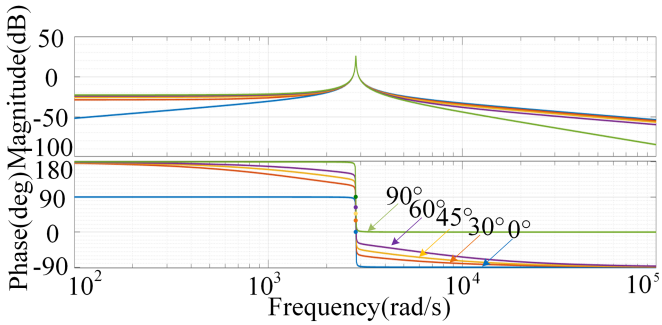

Fig. 11. Bode diagram of PCMPR controller.

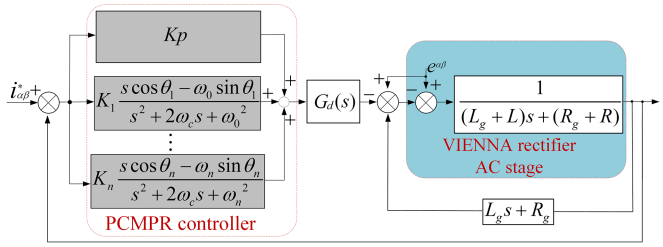

Fig. 12. Transfer function block diagram of the current inner loop with PCMPR controller under weak grid.

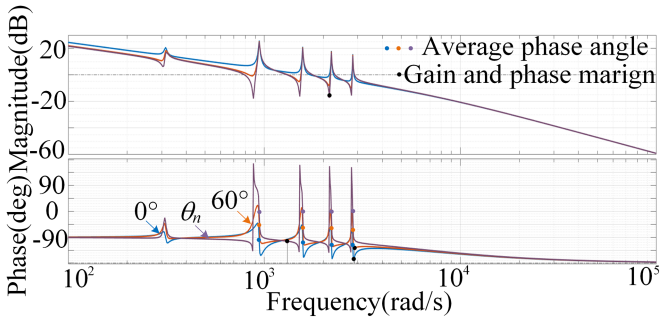

Fig. 13. Bode diagram of PCMPR controllers with different compensate angles.

of proportional differential compensation can be expressed as

$$R(s) = \frac{2K_{r1}\omega_c s^2 + 2K_{r2}\omega_c s}{s^2 + 2\omega_c s + \omega_0^2} \tag{22}$$

where ω_0 is the resonant frequency and K_{r1} and K_{r2} denote the gain of resonant controller.

The phase lag of the control system is mainly caused by the controlled object at low frequency. At high frequencies, the phase lag of the system is jointly affected by the controlled object and the digital control delay as the increasing influence of digital control delay. If only considering the controlled object, formula (22) can be simplified as

$$R(s) = \frac{2K_r\omega_c s(Ls + R)}{s^2 + 2\omega_c s + \omega_0^2}. \tag{23}$$

The bode diagrams of the resonant controller and the resonant controller with the proportional differentiation are shown in Fig. 10. It can be seen that the average phase angle of the resonant controller with proportional differentiation is raised. However, the phase lag caused by the digital control delay cannot be ignored as the frequency increases. And the stability of the system will be challenged when higher resonance controllers are paralleled into the control system.

The PCMPR controller designed in this article can make up for the shortcomings of the abovementioned two phase compensation methods. The PCMPR can be expressed as

$$G(s) = K_p + \sum K_n \frac{s\cos\theta_n - \omega_n \sin\theta_n}{s^2 + 2\omega_c s + \omega_n^2}, n = 1, 3, 5 \ldots \tag{24}$$

when $\omega = \omega_n$, the molecular term of the multiresonance controller is

$$A(s)|_{s=j\omega_n} = \omega_n e^{j\left(\frac{\pi}{2}+\theta_n\right)}. \tag{25}$$

The phase angle of (25) is $\pi/2 + \theta_n$. When ${\omega_n}^- < \omega_n$, the denominator of the phase angle is 0, and the phase angle of the multiresonance controller is $\pi/2 + \theta_n$. When ${\omega_n}^+ > \omega_n$, the denominator of the phase angle is π, and the phase angle of the multiresonance controller is $-\pi/2 + \theta_n$. Therefore, the multiresonance controller has a phase angle transition of π at the resonant frequency ω_n, so its average phase angle can be expressed as

$$\theta_a = \frac{\frac{\pi}{2} + \theta_n - \frac{\pi}{2} + \theta_n}{2} = \theta_n. \tag{26}$$

Fig. 11 shows the PCMPR bode diagram, where the $\omega_c = 10$, $\omega_9 = 900\pi$, $K_9 = 200$, and the compensation angles are, respectively, 0°, 30°, 45°, 60°, 90°. It can be seen that the phase compensated resonance controller can compensate the phase angle to desired angle. And it is the same as the resonance controller with proportional differentiation, which compensates for the phase of the full frequency band. Therefore, the phase angle that the system needs to compensate can be calculated by analyzing the phase lag angle caused by controlled object and digital control delay.

Fig. 12 shows the transfer function block diagram of the current inner loop with PCMPR controller under weak grid. $G_d(s)$ stands for the delay in digital control system including computation delay and PWM delay which can be simplified

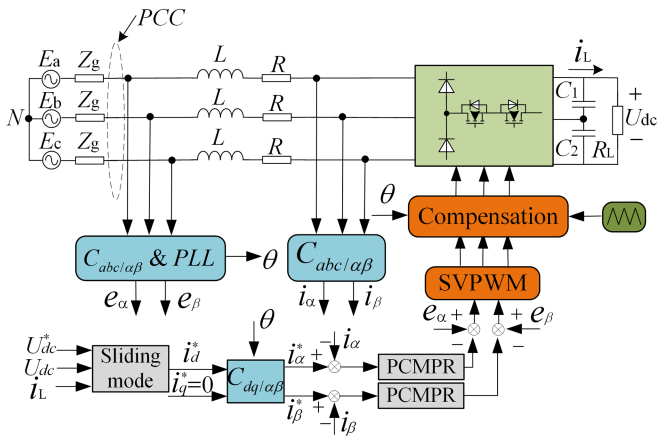

Fig. 14. Block diagram of the control strategy.

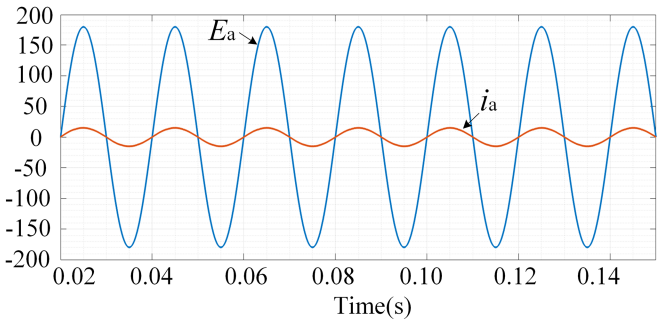

Fig. 15. Input voltage E_a and Input current i_a during stable operation.

3Ts/2 and the function is given as

$$G_d(s) = \frac{1}{Ts + 1}. \tag{27}$$

The controlled object can be equivalent to $G_c(s)$ in both ideal grid and weak grid and the function is given as

$$G_c(s) = \frac{1}{L_z s + R_z}. \tag{28}$$

According to (27), the phase lag angle caused by digital control delay is

$$\theta_1 = -\arctan(T\omega). \tag{29}$$

The sum of the general PWM update delay and calculation delay is $T = 3Ts/2$, T_s is small, and $y = arctan(x)$ can be approximately $y = x$ when the value of x is small. Therefore, the phase lag angle caused by the simplified digital control delay is

$$\theta_1 = -\frac{3}{2}T_s\omega. \tag{30}$$

Similarly, the phase lag angle caused by the controlled object is

$$\theta_2 = -\arctan\left(\frac{L\omega}{R}\right) \tag{31}$$

where $L\omega/R$ is large since the inductance resistance R is very small, and $y = arctan(x) = \pi/2$ due to the x value is large.

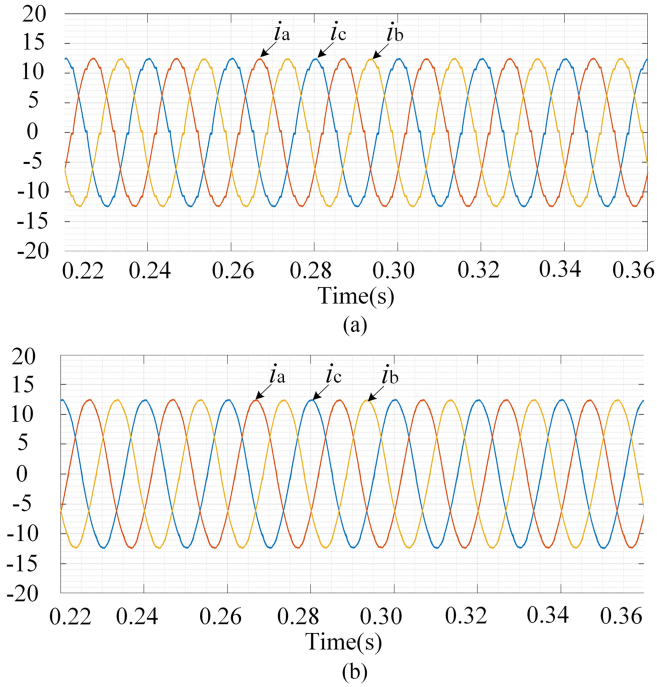

Fig. 16. Input current of Vienna rectifier. (a) Conventional SVPWM. (b) Improved SVPWM.

TABLE II
PARAMETERS OF VIENNA RECTIFIER

Parameter	Value
Input Voltage/(V)	110
frequency/(HZ)	50
Inductance value/(mH)	2.5
Output voltage/(V)	360
Switching frequency/(kHZ)	10
Load/(Ω)	100

Therefore, the phase lag angle caused by digital control delay and controlled object is

$$\theta_l = -\left(\frac{\pi}{2} + \frac{3}{2}T_s\omega\right). \tag{32}$$

According to the abovementioned analysis, considering the calculation delay and PWM update delay, the compensation angle θ_n can be calculated as follows:

$$\theta_n = \frac{\pi}{2} + \frac{3}{2}\omega_n T_s, n = 1, 3, 5 \ldots. \tag{33}$$

Fig. 13 shows the bode diagram of PCMPR controller with different compensate angles. In Fig. 13, the average phase angle of the system at the resonant frequency is marked by colored dots, and the phase margin of the system is marked by black dots. When the compensate angle $\theta = 0°$, the expression of PCMPR controller and multiresonance controller is the same, and the phase margin of the system is 15.4°; When the compensate angle $\theta = 60°$, the phase margin of the system is 52.9°; When the compensate angle $\theta = \theta_n$, the phase margin of the system is 76.4°. It can be clearly seen that the average phase

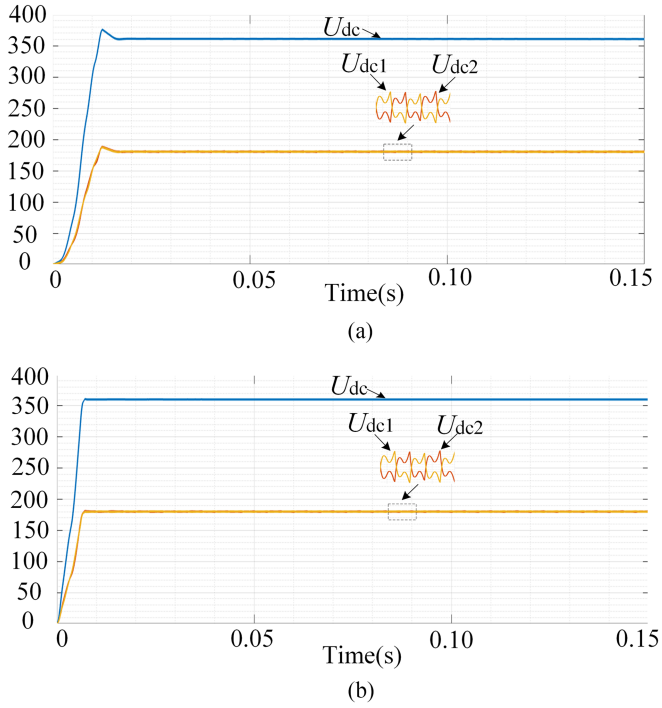

Fig. 17. Output voltage U_{dc} of Vienna rectifier. (a) With PI control. (b) With sliding mode control.

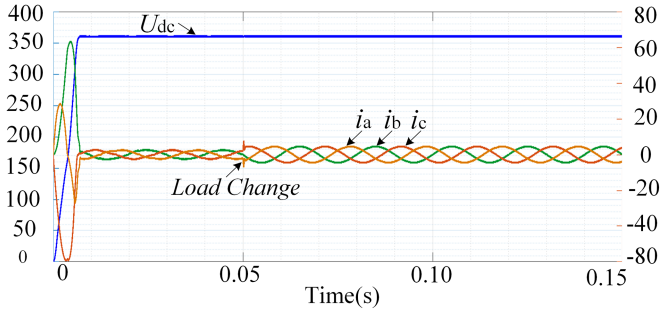

Fig. 18. Output voltage and input current under load mutation.

angle is significantly compensated with the PCMPR controller, and the phase margin increases, so the stability of the rectifier system is improved. Compared with the lead compensator and proportional differential compensator, the PCMPR controller has the following advantages.

1) No need to add additional controllers, reducing the complexity of parameter design.
2) It can compensate the phase of the whole frequency band.
3) It does not affect the gain of the control system at the resonant frequency.
4) It can compensate for the phase lag caused by the controlled object and the digital control delay.

B. Design of Voltage Controller

The dynamic response of Vienna rectifier system is slow under traditional PI control and the rectifier system is easy to overshoot. To improve the dynamic response and suppress voltage overshoot, the voltage controller is designed by using

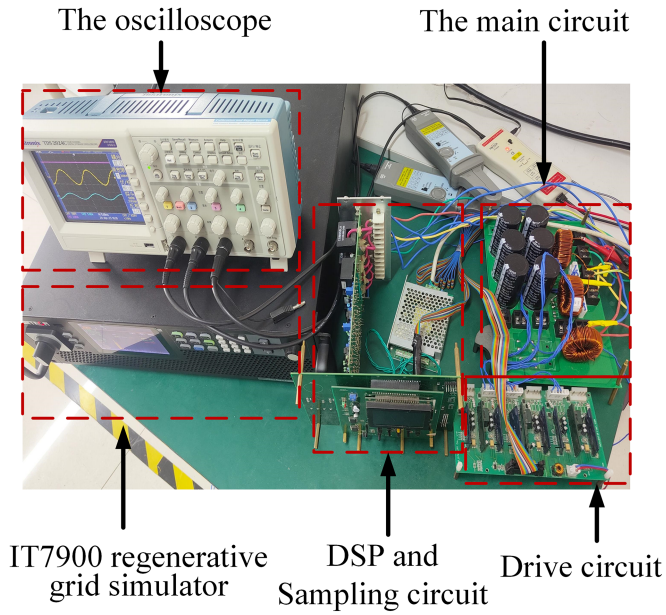

Fig. 19. Experimental prototype of the Vienna rectifier.

sliding mode control. The output of voltage controller is the current reference $i_d{}^*$ on d-axis.

U_{dc} and i_q are variables of the sliding mode control, and the equation is established as follows:

$$\begin{bmatrix} S_1 \\ S_2 \end{bmatrix} = \begin{bmatrix} i_q^* - i_q \\ U_{dc}^* - U_{dc} \end{bmatrix} \tag{34}$$

where S_1 and S_2 are the selected sliding mode surfaces.

Assume that the Vienna rectifier system operates at a unit power factor, S_1 is equal to 0, and the derivative of U_{dc} can be written as

$$\dot{S}_2 = -\frac{dU_{dc}}{dt}. \tag{35}$$

Substituting (6) into (35), it can be obtained

$$\dot{S}_2 = -\frac{dU_{dc}}{dt} = -\frac{3}{2C}\left(S_d i_d + S_q i_q\right) + \frac{4}{2C} i_L \tag{36}$$

where S_d and S_q are the switching functions in dq coordinate system, the S_d and S_q can be expressed as

$$\begin{cases} S_d = \frac{2\left(E_d - Ri_d + \omega L i_q - L\frac{di_d}{dt}\right)}{U_{dc}} \\ S_q = \frac{2\left(E_q - Ri_q - \omega L i_d - L\frac{di_q}{dt}\right)}{U_{dc}}. \end{cases} \tag{37}$$

In order to minimize chattering near the sliding mode surface, the sliding mode controller is designed by using index reaching law, it can be expressed as

$$\dot{s} = -k_0 S - \varepsilon_0 \operatorname{sgn} S. \tag{38}$$

However, the parameters of the conventional index approaching law are constant, so the system will still chatter when approaching the sliding surface. Therefore, the variable index

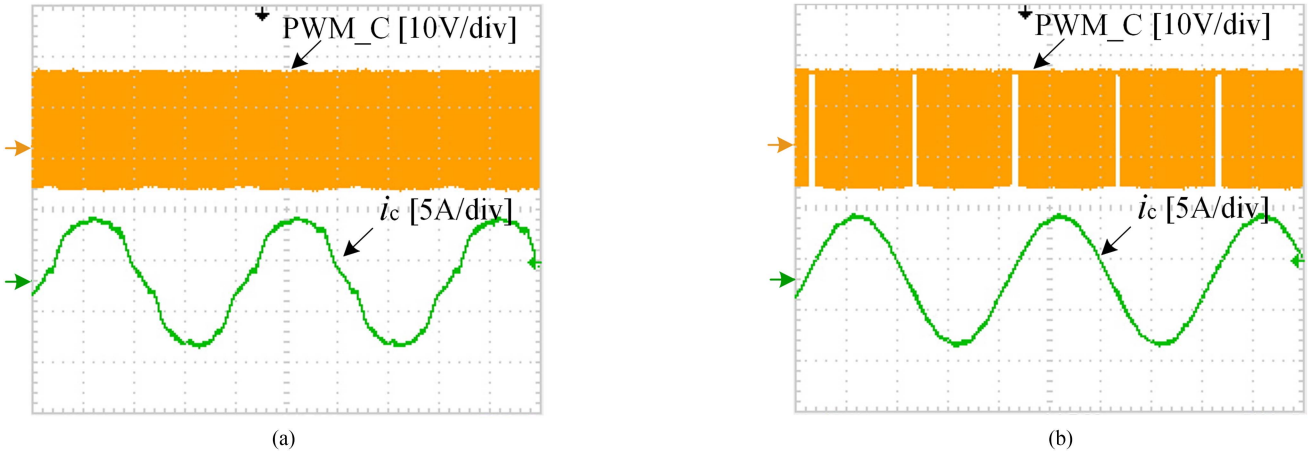

Fig. 20. Input current i_c of Vienna rectifier and its switching waveforms. (a) With conventional SVPWM. (b) With the improved SVPWM.

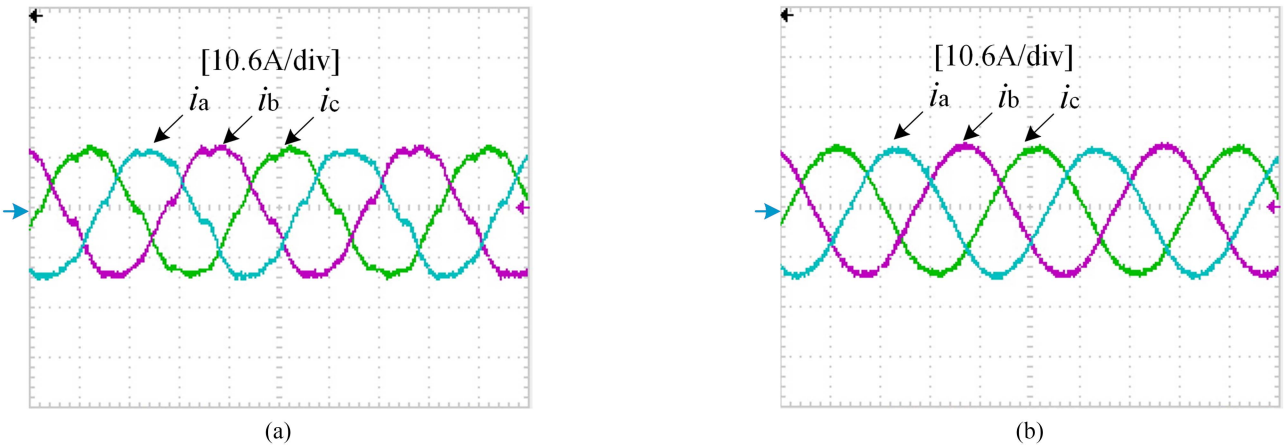

Fig. 21. Three-phase input currents of Vienna rectifier. (a) With conventional SVPWM. (b) With the improved SVPWM.

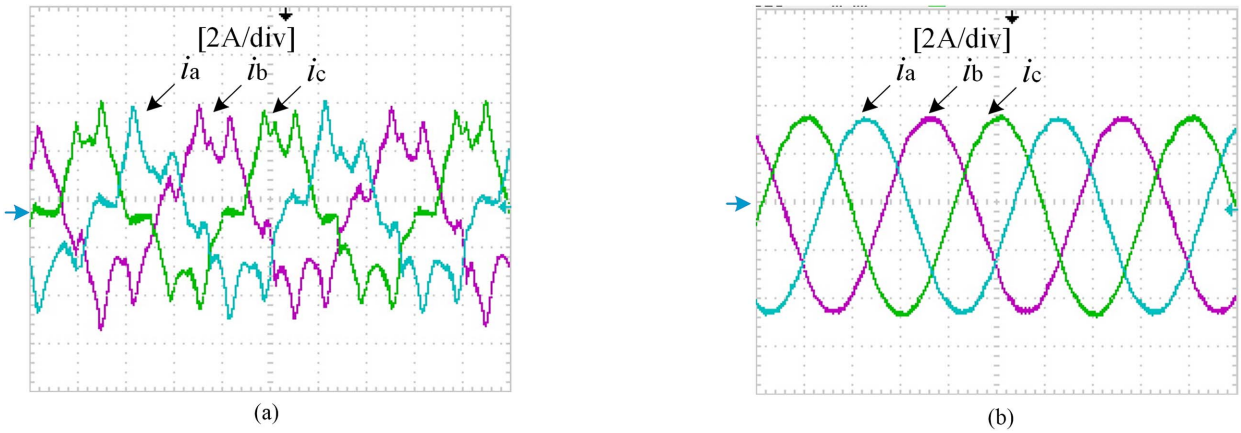

Fig. 22. Three-phase input currents of Vienna rectifier. (a) With the MPR parallel 3rd, 5th, 7th, 9th resonant controllers. (b) With the PCMPR parallel 3rd, 5th, 7th, 9th,11th, 13th, 15th resonant controllers.

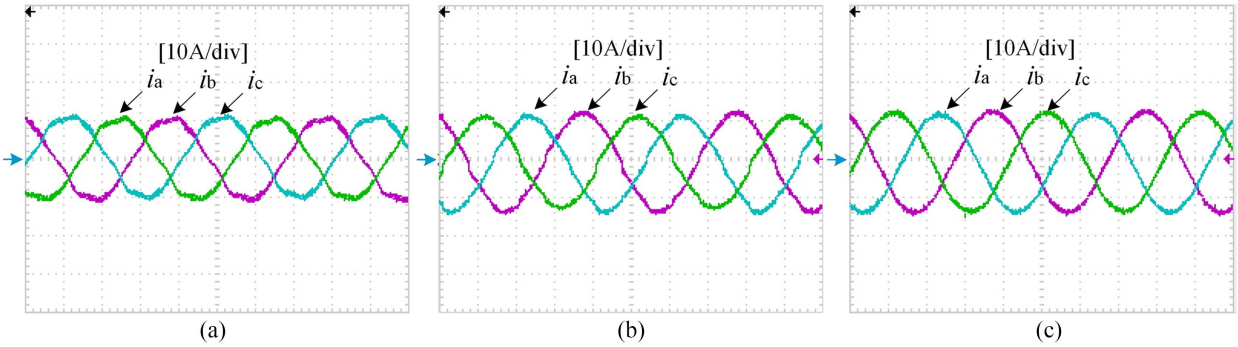

Fig. 23. Input currents of Vienna rectifier and their harmonics spectra. (a) With PI controller. (b) With PR controller. (c) With PCMPR controller.

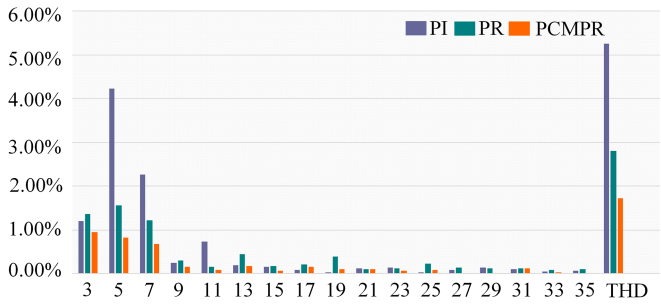

Fig. 24. Harmonic distortions spectra for input currents i_{a} with different control strategies.

approaching law proposed in this article is as follows:

$$\dot{s} = -k_0 S - \left(\frac{2^{|S|}}{2^{|S|}+1} - \frac{1}{2}\right)\varepsilon_0 \operatorname{sgn} S. \tag{39}$$

The parameters of the variable index approaching law are varied, when the system state is far from the sliding surface, the parameter k_0 has the main effect of allowing the system to quickly approach given value. When it reaches near the given value, $k_0 S$ approaches to zero and the second term plays the main role. Since the parameter of the second term is variable, when the control error of the system is zero, the parameter of the second term can also be zero. Therefore, the variable index approaching law can prevent the system from chattering near the sliding surface.

When the system is in steady state, the inductor voltage is close to zero, and the current value of the q-axis is zero. Therefore, by combining the abovementioned formulas, the given value of d-axis current $i_{\mathrm{d}}{}^*$ can be expressed as

$$i_d^* = \left[k_0 S_2 + \left(\frac{2^{|S_2|}}{2^{|S_2|}+1} - \frac{1}{2}\right)\varepsilon_0 \operatorname{sgn} S_2 + \frac{2}{C} i_L\right] \times \frac{C U_{\mathrm{dc}}}{3(E_d - R i_d)}. \tag{40}$$

As can be seen from the formula (40), the reference current $i_{\mathrm{d}}{}^*$ required can be calculated by the dc reference voltage $\mathrm{U_{dc}}{}^*$, dc output voltage U_{dc}, and output current i_{L}. It should be noted that when the Vienna rectifier is operated under weak grid, the expressions for the given values of d-axis currents $i_{\mathrm{d}}{}^*$ is not changed. However, since the three-phase voltage contains a large number of harmonics, the voltage component on the d-axis E_{d} also has a harmonic component. In order to enhance the stability of the system, E_{d} is the d-axis voltage after filtering out the harmonics. The closed-loop control strategy proposed in this article is shown in Fig. 14.

V. Simulation and Experimental Results

A. Simulation Results

To verify the effectiveness of the proposed method, a simulation model is built in MATLAB/Simulink.

Fig. 15 shows the steady-state input voltage E_{a} and input current i_a of the Vienna rectifier with unit power factor. Fig. 16(a) shows the input current with conventional SVPWM. The current has obvious distortion, which will cause the current harmonics to increase. As shown in Fig. 16(b), the zero-crossing distortion of input current with the improved SVPWM is suppressed effectively, hence, the effectiveness of the improved modulation strategy is proved.

Fig. 17(a) shows the dynamic response of the output voltage U_{dc} of voltage outer loop with PI control. It can be seen that the output voltage has obvious overshoot and the system reaches the given value after 0.018 s. Fig. 17(b) shows the dynamic response of the output voltage U_{dc} of voltage outer loop with sliding mode control. The system reaches stability after 0.008 s, and the voltage U_{dc} has no obvious overshoot. It is verified that the dynamic performance of sliding mode control is obviously better than the dynamic performance of PI control.

Fig. 18 shows the dynamic responses of output voltage and grid-side current under abrupt load change with sliding mode control. When the load changes from 100 Ω to 50 Ω at 0.05 s, the VIENNA rectifier enters into a new steady state after 0.01 s.

B. Experimental Results

To evaluate the modulation and control strategy under ideal grid and weak grid, a 1.5 KW experimental system was built as shown in Fig. 19. By using IT7900 regenerative grid simulator the ideal grid is injected with harmonics to simulate the weak grid. The control system mainly consists of DSPF28335. The sampling chip model is AD7656-1, the voltage sensor is

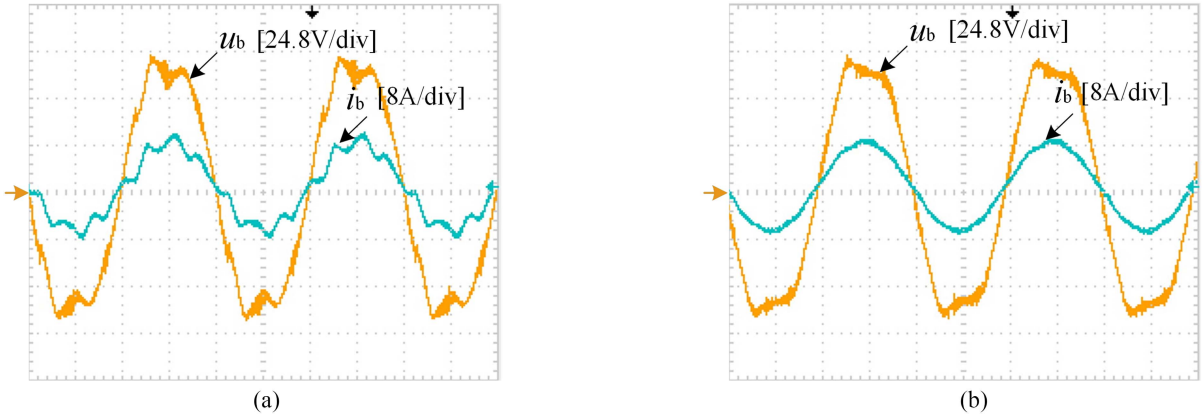

Fig. 25. Input voltage U_b and input current i_b of Vienna rectifier under weak grid with different modulation strategies. (a) With conventional SVPWM. (b) With the improved SVPWM.

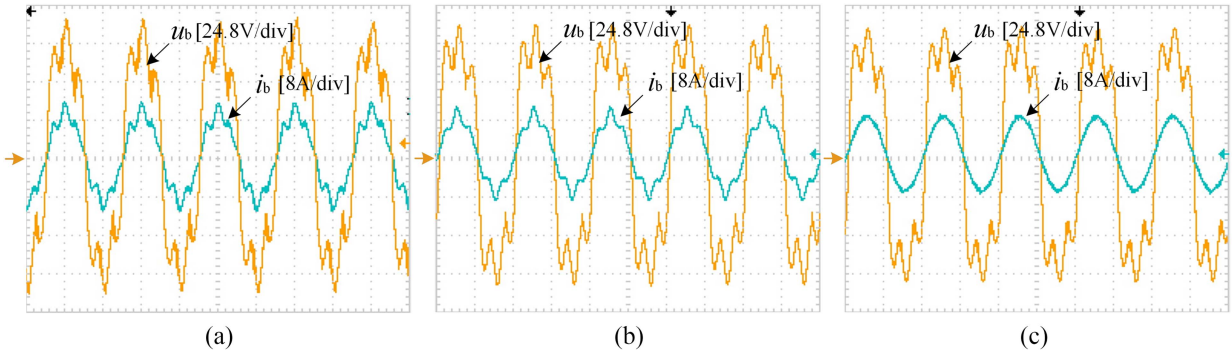

Fig. 26. Input voltage U_b and input current i_b of Vienna rectifier under weak grid with different control strategies. (a) With PI controller. (b) With PR controller. (c) With PCMPR controller.

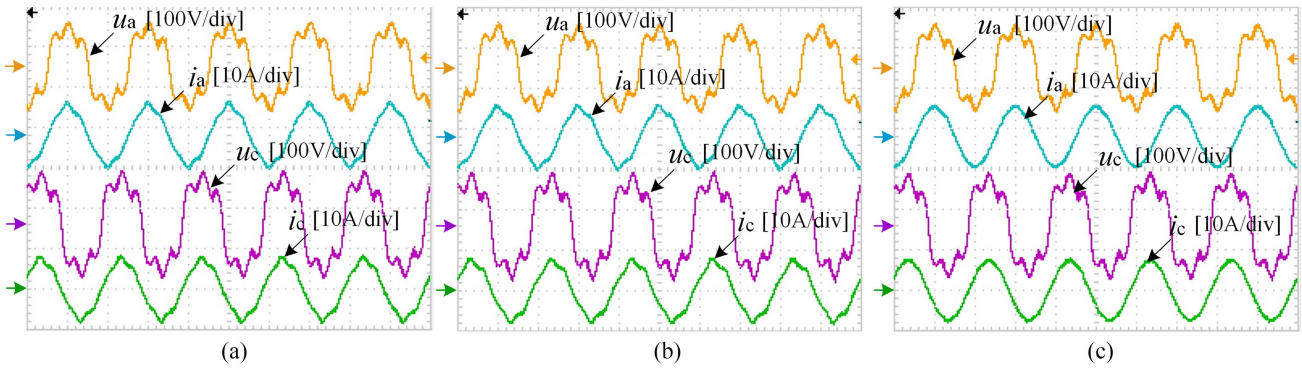

Fig. 27. Input voltage U_a,U_c and input current i_a,i_c of Vienna rectifier under unbalance weak grid with different control strategies. (a) With PI controller. (b) With PR controller. (c) With PCMPR controller.

VSM025A, and the voltage sensor is CSM050LA. And the parameters are given in Table II.

As shown in Fig. 20(a), the switching waveforms with conventional SVPWM near the current zero-crossing point is not clamped to zero, leading to the appearance of zero-crossing distortion. It can be seen that the switching waveforms with the improved SVPWM near the current zero-crossing point is clamped to zero and zero-crossing distortion does not appear in Fig. 20(b).

Fig. 21(a) shows the waveforms of three-phase input currents using conventional SVPWM and Fig. 21(b) shows the waveforms of three-phase input currents using the improved SVPWM. When using the improved SVPWM, the zero crossing distortion is suppressed.

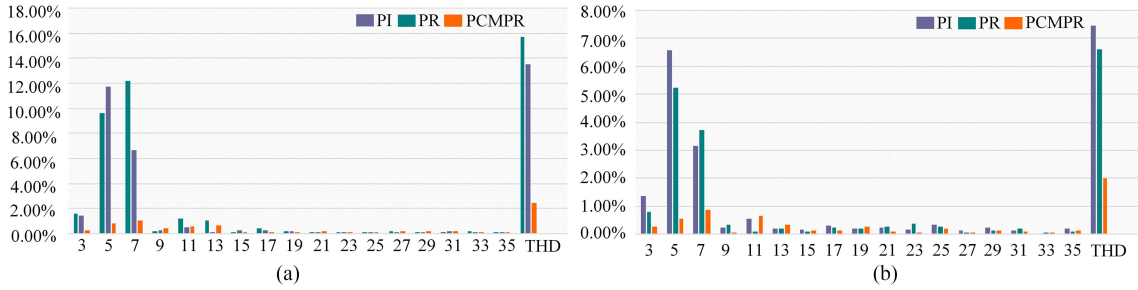

Fig. 28. Harmonic distortions spectra for input currents with different control strategies under weak grid and unbalance weak grid. (a) Under weak grid. (b) Under unbalance weak grid.

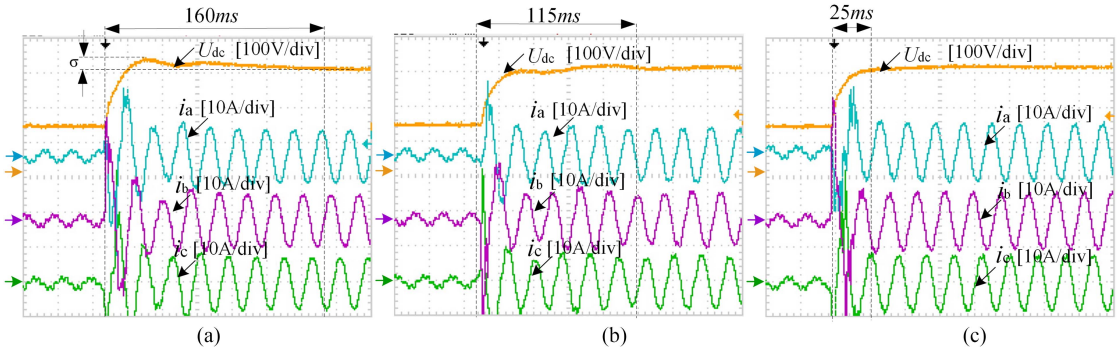

Fig. 29. Input current i_a, i_b, i_c and output voltage U_{dc} of Vienna rectifier at startup with different voltage controllers. (a) PI controller. (b) Sliding mode controller with traditional approaching law. (c) Sliding mode controller with variable index approaching law.

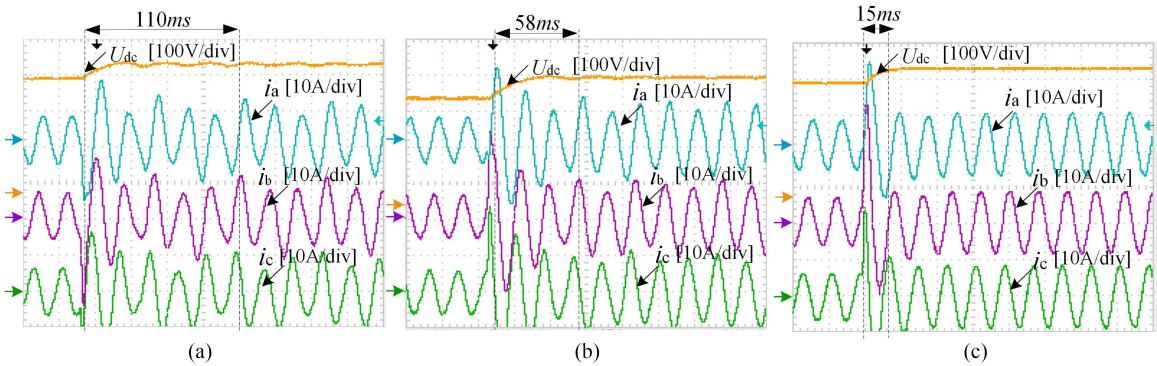

Fig. 30. Input current i_a, i_b, i_c and output voltage U_{dc} of Vienna rectifier under the reference voltage mutation with different voltage controllers. (a) PI controller. (b) Sliding mode controller with traditional approaching law. (c) Sliding mode controller with variable index approaching law.

Fig. 22 shows the input current of the VIENNA rectifier under the multiresonance controller and PCMPR controller. When the multiresonance controller parallels third, fifth, seventh, ninth resonant controllers, the system becomes unstable because of the phase lag. When the PCMPR controller parallels 3rd, 5th, 7th, 9th,11th, 13th, 15th resonant controllers, the system is stable and current harmonics are suppressed.

Fig. 23(a) shows the three-phase input currents with the PI controller, Fig. 23(b) shows the three-phase input currents with the PR controller, Fig. 23(c) shows the three-phase input currents with the current inner loop controlled by PCMPR parallel 3rd, 5th, 7th, 9th,11th, 13th, 15th resonant controllers, it is clear that the THD of the input current with PCMPR is smaller than with PI and PR controllers. As shown in Fig. 24, the odd harmonics of input currents with PI, PR controllers have a magnitude larger than those with PCMPR control. The THD of input currents with PI controller is 5.258%, The THD of input currents with PR controller is 2.806%, and the THD of input currents with PCMPR controller is 1.722%. It proves that the steady-state performance of the rectifier system has been improved with PCMPR controller.

In order to verify the effectiveness of the modulation strategy under weak grid, the 3rd harmonic was injected by using IT7900 regenerative grid simulator, and its relative amplitudes

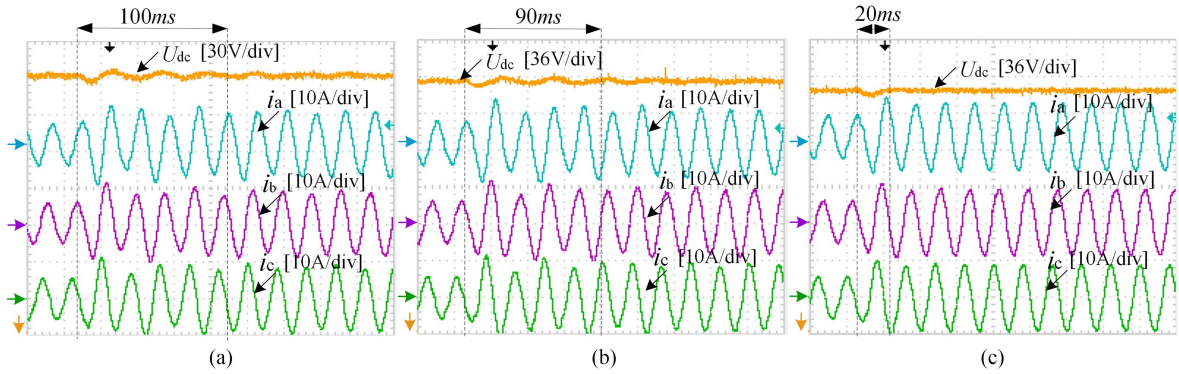

Fig. 31. Input current i_a, i_b, i_c and output voltage U_{dc} of Vienna rectifier under load mutation with different voltage controllers. (a) PI controller. (b) Sliding mode controller with traditional approaching law. (c) Sliding mode controller with variable index approaching law.

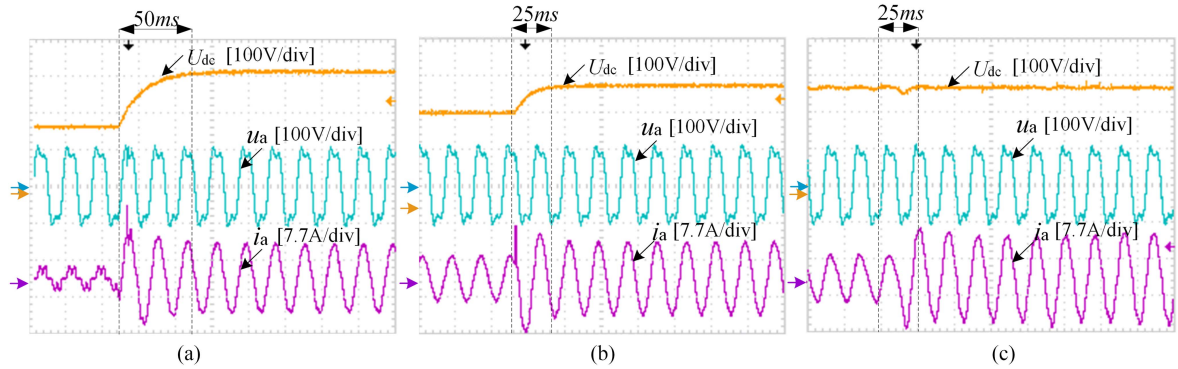

Fig. 32. Input current i_a, i_b, i_c and output voltage U_{dc} of Vienna rectifier under weak grid with sliding mode controller based on variable index approaching law and PCMPR controller. (a) Waveforms of startup. (b) Waveforms of reference voltage mutation. (c) Waveforms of load mutation.

of the fundamental waveform is 24.5%. As shown in Fig. 25, the improved SVPWM can still suppress current zero-crossing distortion under the weak grid.

In order to verify the effectiveness of the closed-loop control strategy under weak grid, the 3rd, 5th, 7th, 9th,11th, 13th, 15th harmonics were injected by using IT7900 regenerative grid simulator, and their relative amplitudes of the fundamental waveforms are 15%, 10%, 3%, 2%, 1%, 1%, 1%, respectively. Fig. 26 shows the input voltage u_b and input current i_b of VIENNA rectifier under balanced weak grid with different control strategies. As shown in Fig. 28(a), the THD of input current i_b under balanced weak grid with PI controller, PR controller, and PCMPR controller are 15.695%, 13.535%, and 2.409%, respectively.

Fig. 27 shows the input voltages u_a, u_c and input currents i_a, i_c of Vienna rectifier under unbalanced weak grid with different control strategies. The rms value of input voltage u_a u_b are 75 V, and the rms value of u_c is 95 V. Fig. 28(b) shows the harmonic distortions spectra for input current i_c, the THD of input current i_c under unbalanced weak grid with PI controller, PR controller, and PCMPR controller are 7.471%, 6.620%, and 1.988%, respectively. The experimental results in Figs. 26–28 verify that PCMPR controller can effectively suppress input current harmonics under weak grid.

Fig. 29 shows the output voltage U_{dc} and the three-phase input currents i_a, i_b, i_c at startup with different voltage loop controllers. As shown in Fig. 29(a), the output voltage U_{dc} of the system with PI controller has a significant overshoot. Fig. 29(b) shows that the output voltage U_{dc} oscillates significantly with the control effect of sliding mode control based on traditional approaching law. Fig. 29(c) shows the experimental waveforms with sliding mode control based on variable index approaching law, the output voltage U_{dc} has no oscillation and the system enters a new steady state after 25 ms. Fig. 30 shows the output voltage U_{dc} and the three-phase input currents i_a, i_b, i_c under reference voltage mutation under different voltage loop controllers. As shown in Fig. 30(a) and (b), the system takes a long time to enter a new steady state with the PI controller and sliding mode controller based on traditional approaching law.

As shown in Fig. 30(c), the system enters a new steady state about 20 ms with the sliding mode control based on variable index approaching law. Fig. 31 shows the output voltage U_{dc} and the three-phase input currents i_a, i_b, i_c under load mutation with different voltage loop controllers. Similar to Figs. 29 and 30, the output voltage U_{dc} has obvious oscillation under PI controller and sliding mode controller based on traditional approaching law, and the system enters the stable state after 100 ms and 90 ms, respectively. When the voltage loop is the sliding mode controller based on variable index approaching law, the system only needs about 20 ms to enter the stable state, and the oscillation does not occur. Fig. 32 shows the output voltage U_{dc} and the three-phase input currents i_a, i_b, i_c under weak grid

with the closed-loop control strategy designed in this article. It can be seen in Fig. 32 that in the case of weak grid, there is no overvoltage and oscillation phenomenon with the control strategy proposed in this article.

VI. Conclusion

In this article, an improved SVPWM modulation for Vienna rectifier has been proposed. In the proposed design, the modulation waveforms of Vienna rectifier near current zero-crossing point is clamped to zero to eliminate zero-crossing distortion. Moreover, the sliding mode controller based on variable index approaching law is proposed in the outer voltage loop to improve the dynamic response performance and reduce the chatter of the output voltage near the sliding surface. In the current inner loop, by comparing other phase compensation methods, the PCMPR controller is adopted to reduce the THD of the input current and improve the phase margin. And by analyzing the closed-loop system control block diagram of the Vienna rectifier, the compensation phase angle of each resonant controller is calculated. Finally, the correctness and effectiveness of the proposed control scheme are verified by simulation and experiment results under both ideal and weak grids.

References

[1] F. Nejabatkhah, Y. W. Li, and H. Tian, "Power quality control of smart hybrid AC/DC microgrids: An overview," *IEEE Access*, vol. 7, pp. 52295–52318, 2019, doi: 10.1109/ACCESS.2019.2912376.

[2] G. Rajendran, C. A. Vaithilingam, N. Misron, K. Naidu, and M. R. Ahmed, "Voltage oriented controller based Vienna rectifier for electric vehicle charging stations," *IEEE Access*, vol. 9, pp. 50798–50809, 2021, doi: 10.1109/ACCESS.2021.3068653.

[3] J. Gu, X. Chen, R. Li, B. Liu, and N. Zheng, "Improved one cycle control for three-phase three-wire VIENNA rectifier," in *Proc. IEEE Workshop Wide Bandgap Power Devices Appl. Asia*, 2021, pp. 296–301, doi: 10.1109/WiPDAAsia51810.2021.9656067.

[4] M. Hagemeyer, P. Wallmeier, F. Schafmeister, and J. Böcker, "Comparison of unidirectional three- and four-wire-based boost PFC-rectifier topologies for non-isolated three-phase EV on-board chargers under common-mode aspects," in *Proc. IEEE Appl. Power Electron. Conf. Expo.*, 2021, pp. 569–576, doi: 10.1109/APEC42165.2021.9487036.

[5] M. Darnet, E. Godoy, C. Karimi, and S. Gautrais, "Input currents DCM modelling of a Vienna-based rectifier," in *Proc. IEEE Conf. Control Technol. Appl.*, 2021, pp. 589–594, doi: 10.1109/CCTA48906.2021.9659229.

[6] B. Zhang, C. Zhang, X. Xing, X. Li, and Z. Chen, "Novel three-layer discontinuous PWM method for mitigating resonant current and zero-crossing distortion in Vienna rectifier with an LCL filter," *IEEE Trans. Power Electron.*, vol. 36, no. 12, pp. 14478–14490, Dec. 2021, doi: 10.1109/TPEL.2021.3088610.

[7] J. Wang, S. Ji, S. Liu, H. Jiang, and W. Jiang, "A discontinuous PWM strategy to control neutral point voltage for Vienna rectifier with improved PWM sequence," *IEEE J. Emerg. Sel. Topics Power Electron.*, vol. 10, no. 3, pp. 3230–3241, Jun. 2022, doi: 10.1109/JESTPE.2021.3120540.

[8] L. Song, S. Duan, R. Li, X. Liu, and B. Ji, "A hybrid discontinuous PWM strategy for current ripple and neutral-point fluctuation reduction of parallel Vienna rectifier," *IEEE Trans. Ind. Electron.*, vol. 70, no. 3, pp. 2531–2542, Mar. 2023, doi: 10.1109/TIE.2022.3170618.

[9] L. Zhang et al., "A modified DPWM with neutral point voltage balance capability for three-phase Vienna rectifiers," *IEEE Trans. Power Electron.*, vol. 36, no. 1, pp. 263–273, Jan. 2021, doi: 10.1109/TPEL.2020.3002660.

[10] A. Sunbul and V. K. Sood, "Simplified SVPWM method for the Vienna rectifier," in *Proc. 20th Workshop Control Model. Power Electron.*, 2019, pp. 1–8, doi: 10.1109/COMPEL.2019.8769689.

[11] H. Cheng and J. Huang, "Research on SVPWM control strategy of three phase VIENNA rectifier," in *Proc. 5th Int. Conf. Syst. Inform.*, 2018, pp. 166–170, doi: 10.1109/ICSAI.2018.8599384.

[12] W. Yao, Z. Lv, M. Zhang, and Z. Lin, "A novel SVPWM scheme for Vienna rectifier without current distortion at current zero-crossing point," in *Proc. IEEE 23rd Int. Symp. Ind. Electron.*, 2014, pp. 2349–2353, doi: 10.1109/ISIE.2014.6864986.

[13] Z. Miao, H. Tong, X. Jin, W. Yao, Z. Lu, and Z. Ma, "DQ-frame zero-crossing effect modeling and current distortion compensation method for Vienna rectifier," *IEEE Trans. Power Electron.*, vol. 35, no. 7, pp. 7612–7623, Jul. 2020, doi: 10.1109/TPEL.2019.2957540.

[14] T. Wang, C. Chen, P. Liu, T. Liu, Z. Chao, and S. Duan, "A hybrid space-vector modulation method for harmonics and current ripple reduction of interleaved Vienna rectifier," *IEEE Trans. Ind. Electron.*, vol. 67, no. 10, pp. 8088–8099, Oct. 2020, doi: 10.1109/TIE.2019.2947810.

[15] K. Y. Ahmed, N. Z. Bin Yahaya, V. S. Asirvadam, N. Saad, R. Kannan, and O. Ibrahim, "Development of power electronic distribution transformer based on adaptive PI controller," *IEEE Access*, vol. 6, pp. 44970–44980, 2018, doi: 10.1109/ACCESS.2018.2861420.

[16] Y. Li and H. Zhao, "A space vector switching pattern hysteresis control strategy in VIENNA rectifier," *IEEE Access*, vol. 8, pp. 60142–60151, 2020, doi: 10.1109/ACCESS.2020.2977656.

[17] J.-S. Lee, K.-B. Lee, and F. Blaabjerg, "Predictive control with discrete space-vector modulation of Vienna rectifier for driving PMSG of wind turbine systems," *IEEE Trans. Power Electron.*, vol. 34, no. 12, pp. 12368–12383, Dec. 2019, doi: 10.1109/TPEL.2019.2905843.

[18] X. Li, Y. Sun, H. Wang, M. Su, and S. Huang, "A hybrid control scheme for three-phase Vienna rectifiers," *IEEE Trans. Power Electron.*, vol. 33, no. 1, pp. 629–640, Jan. 2018, doi: 10.1109/TPEL.2017.2661382.

[19] M. Mobarrez, A. Kadavelugu, U. Raheja, and H. Suryanarayana, "A control method for THD minimization in high power density Vienna-type rectifier," in *Proc. IEEE Appl. Power Electron. Conf. Expo.*, 2021, pp. 921–926, doi: 10.1109/APEC42165.2021.9487383.

[20] Z. Ma, X. Zhang, J. Huang, and B. Zhao, "Stability-constraining-dichotomy-solution-based model predictive control to improve the stability of power conversion system in the MEA," *IEEE Trans. Ind. Electron.*, vol. 66, no. 7, pp. 5696–5706, Jul. 2019, doi: 10.1109/TIE.2018.2875418.

[21] Z. Wang, A. Zhang, and H. Zhang, "Research on voltage sliding mode control of Vienna rectifier," in *Proc. Chin. Control Decis. Conf.*, 2020, pp. 251–255, doi: 10.1109/CCDC49329.2020.9164124.

[22] T. Wang, C. Chen, P. Liu, W. Zhu, and S. Duan, "A current control method with extended bandwidth for Vienna rectifier considering wide inductance variation," *IEEE J. Emerg. Sel. Topics Power Electron.*, vol. 9, no. 1, pp. 590–601, Feb. 2021, doi: 10.1109/JESTPE.2019.2946872.

[23] T. Liu, C. Chen, T. Wang, S. Duan, and H. Cheng, "Proportional-resonant current control for VIENNA rectifier in stationary $\alpha\beta$ frame," in *Proc. IEEE Int. Power Electron. Appl. Conf. Expo.*, 2018, pp. 1–7, doi: 10.1109/PEAC.2018.8589971.

[24] L. Hang, B. Li, M. Zhang, Y. Wang, and L. M. Tolbert, "Equivalence of SVM and carrier-based PWM in three-phase/wire/level Vienna rectifier and capability of unbalanced-load control," *IEEE Trans. Ind. Electron.*, vol. 61, no. 1, pp. 20–28, Jan. 2014, doi: 10.1109/TIE.2013.2240637.

[25] A. G. Yepes, F. D. Freijedo, Ó. Lopez, and J. Doval-Gandoy, "High-performance digital resonant controllers implemented with two integrators," *IEEE Trans. Power Electron.*, vol. 26, no. 2, pp. 563–576, Feb. 2011, doi: 10.1109/TPEL.2010.2066290.

[26] T. Wang, C. Chen, T. Liu, Z. Chao, and S. Duan, "Current ripple analysis of three-phase Vienna rectifier considering inductance variation of powder core inductor," *IEEE Trans. Power Electron.*, vol. 35, no. 5, pp. 4568–4578, May 2020, doi: 10.1109/TPEL.2019.2944853.

Wenjie Zhu (Member, IEEE) received the B.Sc. degree from the Jiaozuo Institute of Technology, Jiaozuo, China, in 2002, the M.Sc. degree from Shandong University, Jinan, China, in 2005, and the Ph.D. degree from Southeast University, Nanjing, China, in 2014, all in electrical engineering.

Since 2005, he has been with the Qingdao University of Technology, where he is currently an Associate Professor with the School of Information and Control Engineering. He has authored or coauthored more than 20 technical papers and several granted patents in relevant areas. His research interests include power electronics and electric drives, control of power converters, and renewable energy generation.

Xuewu Li was born in Shandong, China, in 1998. He received the B.Sc. degree in electrical engineering in 2021 from the Qingdao University of Technology, Qingdao, China, where he is currently working toward the M.Sc. degree in electrical information.

His research interests include harmonic suppression, high frequency link dc–ac converters, and accurate rectifier control.

Xiaoya Cao received the B.Sc. degree in electrical engineering and automation from the Qilu University of Technology, Jinan, China, in 2020. She is currently working toward the M.Sc. degree in control science and engineering with the School of Information and Control Engineering, Qingdao University of Technology, Qingdao, China.

Her research interests include modulation and control of dc–ac converters, and high frequency link dc–ac converters.

Yunfei Li was born in Shandong Province, China. He received the Bachelor's degree in electrical engineering and automation from Qingdao University of Technology in Qingdao, China in 2021. He is currently pursuing the master's degree in electronic information at Qingdao University of Technology.

His research interests include power electronics and its precise control, mainly studying high frequency link inverter DC–AC, and its parallel control.

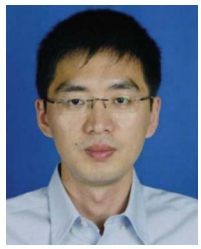

Keliang Zhou (Senior Member, IEEE) received the B.Sc. degree from the Huazhong University of Science and Technology, Wuhan, China, in 1992, the M.Eng. degree from the Wuhan University of Technology, Wuhan, China, in 1995, and the Ph.D. degree from Nanyang Technological University, Singapore, in 2002. all in electrical engineering.

He is currently a Full Professor and the Head with the School of Automation, Wuhan University of Technology. From 2006 to 2019, he was an Academic Staff with Southeast University, China, University of Canterbury, New Zealand, and University of Glasgow, U.K., respectively. He has coauthored one monograph and more than 100 peer-reviewed technical papers, and holds several granted patents in relevant areas. His research interests include modeling and control of power converters, advanced control theory, and applications.